





## Crystal growth and evolution of magnetism in the EuCuP-EuCuAs solid solution

Andrew F. May <sup>1,\*</sup>, Eleanor M. Clements,<sup>1,2</sup> Xiaoping Wang <sup>2</sup>, Heda Zhang <sup>1</sup> and Brenden R. Ortiz <sup>1</sup>

<sup>1</sup>Materials Science and Technology Division, Oak Ridge National Laboratory, Oak Ridge, Tennessee 37831, USA

<sup>2</sup>Neutron Scattering Division, Oak Ridge National Laboratory, Oak Ridge, Tennessee 37831, USA



(Received 18 June 2024; accepted 12 August 2024; published 23 August 2024)

The hexagonal EuMX ( $M = \text{Cu, Ag, Au}$ ;  $X = \text{P, As, Sb, Bi}$ ) compounds host interesting electronic and magnetic properties, with seemingly intertwined topology and transport properties. One key feature of such behavior is the nature of the ordered magnetic structure. In EuCuAs, a topological Hall effect is caused by a conical spin structure that emerges when a field is applied within the easy-plane ( $H \perp c$ ) of the helical ground state that exists below the Neel temperature of  $T_N = 14$  K. On the other hand, EuCuP is an easy-axis ferromagnet with a Curie temperature  $T_C$  near 31 K. Here, we investigate the evolution of the magnetic properties in EuCuAs<sub>1-x</sub>P<sub>x</sub> single crystals with  $0.16 \leq x \leq 0.75$ . Crystals grown by cooling slowly in a Sn flux possessed macroscale inhomogeneity of As/P, particularly for arsenic-rich crystals. However, growth in a Sn flux via an isothermal dwell at 600 °C produced crystals that were homogeneous within the resolution of the probes utilized to investigate these crystals. The unit cell volumes, Curie-Weiss temperatures, and magnetic transitions trend linearly with composition and the magnetic anisotropy is reduced in the alloys. The magnetization data of crystals with  $x = 0.16$  and 0.24 indicate an easy-plane antiferromagnetic ground state while behavior similar to ferromagnetism is observed for crystals with  $x \geq 0.41$ . The temperature-dependent magnetization data possess multiple transitions for compositions near EuCuAs<sub>0.75</sub>P<sub>0.25</sub>, revealing a competition of ground states in this arsenic-rich region of the phase diagram. Neutron diffraction data for EuCuP are also presented as a follow up to previous results that revealed a two-step transition at  $T_C$ ; the observed data were consistent with ferromagnetic order at  $T = 5$  K.

DOI: [10.1103/PhysRevMaterials.8.084410](https://doi.org/10.1103/PhysRevMaterials.8.084410)

### I. INTRODUCTION

The interplay of magnetism and electronic topology presents an interesting and challenging field of study in modern condensed matter physics. The central idea is that magnetic order can impact the band structure and associated surface states in topological materials, which thus facilitates a tuning of the electronics via an applied field [1]. Alternatively, the magnetism itself can manifest topological character, such as in a skyrmion lattice [2], offering additional routes to potential information technologies [3–5]. Fundamental to these efforts is the need to understand what dictates the nature of the magnetic order, thereby allowing for a logical tuning to access desired states. Within this context, experimental studies of emerging materials provide an important baseline for future theoretical developments [6–32] and for guiding the design of new model systems or manipulation of known systems via chemical substitutions or external parameters.

EuCuPn materials with Pn = (P, As, Sb, Bi) are hexagonal systems that possess divalent Eu ions with a large spin  $S = 7/2$  moment residing on a triangular sublattice [33,34]. Mossbauer spectroscopy has evidenced divalent Eu in the isostructural pnictides containing Cu, Ag, or Au, whereas related compounds containing Ni or Pd can possess mixed valent Eu [35]. The Eu layers stack along the  $c$  axis with a

honeycomb network of CuPn between them, as illustrated in the inset of Fig. 1(a). In the broader family of isostructural materials with the ZrBeSi structure type, these honeycomb networks have a strong impact on the Fermi surface, producing Dirac band crossings in some cases [36–44]. Magnetic order on the Eu sublattice can also impact the topology of the electronic structure in these ternary compounds, as shown for EuAgAs and EuCuBi [45,46].

Magnetic order in EuCuPn materials is strongly impacted by the Pn element, with the ordering temperatures decreasing continually as the unit cell volume increases on moving from P to Bi [33,35]. The nature of the magnetic ground state also changes with choice of Pn. In the magnetically ordered state, ferromagnetic coupling within the basal plane is found in EuCuP and EuCuAs (and EuCuSb), and these materials possess a positive Curie-Weiss temperature obtained from fitting the paramagnetic regime to a Curie-Weiss law [33]. Along the  $c$  axis, the moments are ferromagnetically coupled in EuCuP while a helical spin structure is observed in EuCuAs [47–50]; helical order also competes with collinear antiferromagnetic order in EuCuSb [51].

The magnetic anisotropy also depends on Pn, with EuCuP having easy-axis [001] anisotropy while EuCuAs has moments oriented within the basal plane in the ground state. Evidence for these in-plane moments in EuCuAs comes, in part, from the existence of a metamagnetic transition when a magnetic field is applied within the basal plane [49]. It has been shown that this field-induced transition involves

\*Contact author: mayaf@ornl.gov

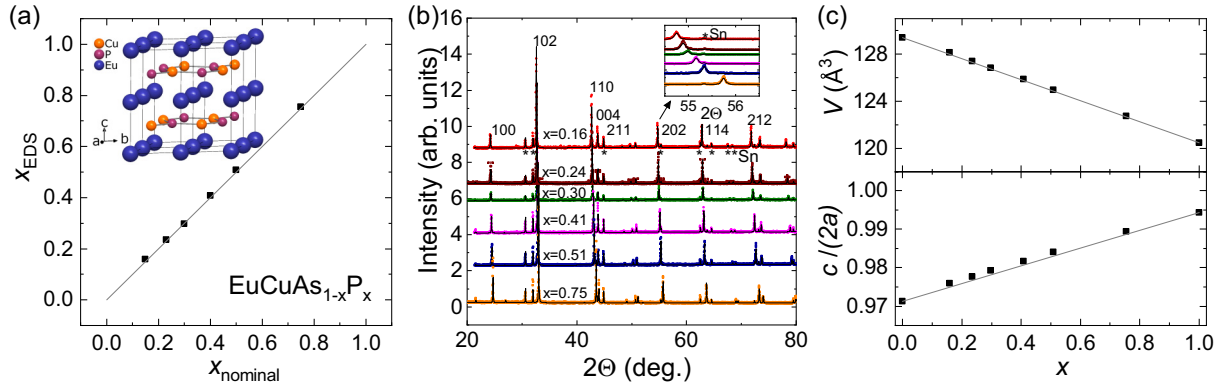


FIG. 1. (a) Experimental composition  $x_{\text{EDS}}$  plotted against the nominal composition of the crystal growths with an inset showing the crystal structure (As at P site). (b) Room temperature powder x-ray diffraction data for pulverized  $\text{EuCuAs}_{1-x}\text{P}_x$  crystals with several Bragg peaks indexed, dominant reflections for tin marked with an asterisk, and an inset showing how the 202 reflection shifts with composition (data stacked vertically in order of main panel). Data are shifted vertically for clarity, and Rietveld refinements are the thin lines. (c) Results from Rietveld refinements plotted versus experimental composition, with the lower panel containing one-half of the  $c/a$  ratio, which equals the ratio of out-of-plane to in-plane Eu-Eu distances (shortest Eu-Eu distances are along [001]).

an evolution from the helical ground state to a conical spin structure that promotes a large topological Hall effect [50]. However, this topological Hall effect is only accessible when the magnetic field is applied within the basal plane, which can be experimentally challenging for such hexagonal crystals that tend to have a platelike morphology. The study reported here was motivated by controlling the anisotropy in these materials via isovalent As/P alloying.

In this work, single crystals in the solid solution series  $\text{EuCuAs}_{1-x}\text{P}_x$  were investigated with an emphasis on understanding how the temperature- and field-dependent magnetic transitions are impacted by composition (lattice volume). Crystals grown out of a tin flux using a traditional slow-cooling method were found to be inhomogeneous, with As/P concentration varying both within and between crystals in a given growth, particularly in As-rich samples. By contrast, crystals grown in a tin flux using an isothermal approach were found to be homogeneous with compositions that nicely match those of the nominal growth compositions, and property data are reported for those crystals. The crystallographic parameters evolve smoothly with composition, as do the magnetic transition temperatures. However, for compositions near  $\text{EuCuAs}_{0.75}\text{P}_{0.25}$  there are multiple temperature-dependent transitions that reveal competing ground states. In addition, we briefly discuss neutron diffraction data for  $\text{EuCuP}$  that are consistent with ferromagnetic order in the ground state; the neutron diffraction experiment was motivated by a two-step transition near the Curie temperature of  $\text{EuCuP}$  [52].

## II. METHODS

Single crystals of  $\text{EuCuAs}_{1-x}\text{P}_x$  were grown using a Sn flux. An isothermal growth was employed to produce homogeneous crystals with experimental compositions that closely track the nominal compositions of the reactions. In the isothermal approach, the mixture of raw elements was first heated at  $60^\circ/\text{h}$  to  $1000^\circ\text{C}$  and held for 12–16 h to allow for dissolution and homogenization. At this point, instead of slowly cooling for crystal growth, the ampoules were removed from the fur-

nace and cooled in air just until the visible red/orange glow faded (approximately 2.5 minutes). The ampoules were then immediately placed into a furnace that was already heated to the growth temperature of  $600^\circ\text{C}$ . Growth of the crystals then occurred in an isothermal condition for at least 860 h, with excess flux removed via centrifugation upon quenching from the growth temperature.

For the growths, high-purity elements were contained inside  $\text{Al}_2\text{O}_3$  crucibles of the Canfield type ( $\text{Al}_2\text{O}_3$  frit-disc filters [53]) that were sealed inside fused silica tubing under vacuum. Eu (rod) was procured from Ames laboratory and used along with red phosphorous lumps, arsenic lumps, and pieces cut from copper slugs. The reactions were loaded in an inert atmosphere glovebox but the products were found to be stable in air. Compositions with varying  $x$  were loaded in the stoichiometry  $7\text{EuCuAs}_{1-x}\text{P}_x : 93\text{Sn}$ ; roughly 4.6 g of Sn was placed in a  $2\text{ cm}^3$  crucible.

X-ray diffraction data were collected using a PANalytical X'Pert Pro MPD with monochromatic  $\text{Cu K}\alpha_1$  ( $\lambda = 1.5406\text{ \AA}$ ) radiation; data for  $x = 0.24$  were obtained without a monochromator and the contribution of  $\text{K}\alpha_2$  was stripped using instrument software. Rietveld refinements were performed using the program FullProf [54]. A Hitachi TM-3000 scanning electron microscope equipped with a Bruker Quantax 70 EDS detector system was utilized to examine the chemical composition of the crystals. The electron beam probes roughly a cubic micron of sample but the EDS data were averaged over tens of microns and the quantification error is estimated to be 1–3 atomic percent. The reported  $x$  values were obtained from the relative P/As concentrations; experimental  $x$  values are utilized unless explicitly noted. Magnetization data were collected using dc squid magnetometry with Quantum Design magnetometers (MPMS-XL and MPMS3). The ac susceptibility data were collected in an MPMS3 using an amplitude of 2 Oe with frequencies ranging from 227.6 to 996.5 Hz; data for  $f = 227.6\text{ Hz}$  are presented herein since a frequency dependence was not observed. Specific heat capacity data were collected using a Quantum Design Physical Property Measurement System

employing both 2% and 30% temperature rises, the latter of which were analyzed using Quantum Design's dual slope analysis routine to capture a high density of data points around the magnetic transitions.

### III. RESULTS AND DISCUSSION

#### A. Characterization of crystal chemistry

We first discuss the impact of the conditions utilized during crystal growth of  $\text{EuCuAs}_{1-x}\text{P}_x$ . Our initial samples were produced by cooling from  $1000^\circ\text{C}$  to  $750^\circ\text{C}$  at  $1\text{--}2^\circ/\text{minute}$  (conditions like those utilized for  $x = 0, 1$  parent compounds we reported upon in Ref. [52]). This slow-cooling approach produced crystals that initially appeared to be of reasonable quality, with sizes similar to that of the  $x = 0, 1$  crystals. Closer inspection revealed that different crystals within one batch sometimes had different  $x$  values, behavior that seemed more prominent for arsenic-rich samples. Further inspection revealed that these growth conditions often produced crystals possessing a concentration gradient. In particular, by comparing EDS results of the as-grown surfaces with those obtained after polishing into the crystal, the surfaces were found to have a higher concentration of arsenic than the interior of the crystals. In some cases, inhomogeneity was also observed across the as-grown (or polished) surface. In addition, individual crystals were ground and measured using powder x-ray diffraction. A splitting and broadening of Bragg peaks was observed in x-ray diffraction data collected on powder obtained by pulverizing an individual crystal (approximately a cubic mm in volume) produced via a slow-cooling approach with a nominal composition of 3  $\text{EuCuAs}_{0.8}\text{P}_{0.2}$  : 97 Sn. This indicates significant chemical inhomogeneity driving a distribution of lattice parameters. The degree of inhomogeneity is likely dependent on the initial flux ratios.

Different ratios of flux to the product content, an indium flux, and an In-Sn flux were explored in attempts to eliminate the chemical inhomogeneity. These efforts focused on arsenic-rich samples (roughly  $x = 0.2$  to  $0.3$ ) due to the observation of interesting magnetic properties near this composition. However, the homogeneity obtained by the different trials utilizing a slow-cooling method was not sufficient to provide confidence during an investigation of the magnetic properties. The concentration gradients within a sample (exterior to interior) indicate a temperature dependence of the relative amounts of As/P in the solid/liquid phases. With five elements in the melt, the roles of solubility are very difficult to gauge. If we just consider the As-Sn and P-Sn binary systems, relatively similar solubility into Sn is observed for the pnictide at the concentrations/temperatures utilized in those growths. Interactions with other species in the melt are likely important in determining the relevant equilibrium constants.

After many slow-cooling growths were completed, it was determined that varying the thermal conditions would provide the best opportunity for obtaining macroscopically homogeneous crystals in a reliable manner. A vast array of conditions exist. To minimize efforts, the isothermal approach was attempted and suitable homogeneity was obtained using a low growth temperature of  $600^\circ\text{C}$ , though crystal masses are small (maximum of  $1\text{--}2$  mg) even at the extended periods utilized.

TABLE I. Results from Rietveld refinement of x-ray diffraction data collected on pulverized  $\text{EuCuAs}_{1-x}\text{P}_x$  crystals at ambient condition and Curie-Weiss temperatures  $\Theta_W$  obtained from fitting data in Fig. 2(a). The refinements are in space group 194 with atoms at the special positions of Eu (0,0,0), Cu ( $\frac{1}{3}, \frac{2}{3}, \frac{3}{4}$ ), As/P ( $\frac{1}{3}, \frac{2}{3}, \frac{1}{4}$ ); As/P concentrations were fixed using the experimental  $x_{\text{EDS}}$  values. The lattice parameters for  $x = 0, 1$  are from Ref. [52].

$x_{\text{EDS}}$	$a$ (Å)	$c$ (Å)	$V$ (Å <sup>3</sup> )	$\Theta_W$ (K)
0 (EuCuAs)	4.2530(1)	8.2614(2)	129.411(4)	20.2(1)
0.16	4.2323(2)	8.2604(3)	128.140(9)	22.6(1)
0.24	4.2213(2)	8.2543(4)	127.384(10)	23.1(1)
0.30	4.2130(2)	8.2512(4)	126.831(13)	25.2(1)
0.41	4.1989(1)	8.2437(3)	125.870(8)	27.6(1)
0.51	4.1854(1)	8.2368(3)	124.956(6)	29.3(1)
0.75	4.1528(1)	8.2176(3)	122.731(6)	32.7(1)
1 (EuCuP)	4.1205(4)	8.1939(9)	120.484(17)	33.6(1)

These results suggest that larger crystals might be produced via optimization of temperature/concentration conditions using a slow-cooling approach over a small temperature window at relatively low temperatures ( $750\text{--}600^\circ\text{C}$ ). This would also be an interesting system to explore an oscillatory growth, with the temperature increasing/decreasing over tens or hundreds of degrees following a quenching protocol similar to that employed for the isothermal conditions reported here.

Diffraction data collected on pulverized crystals from isothermal growths demonstrated macroscopically homogeneous products (no peak splitting), as shown in Fig. 1(b). Consistent with this, EDS inspection did not reveal varying concentrations in the crystals from a given isothermal growth. In addition, the compositions obtained via EDS were very similar to the nominal growth compositions, as illustrated in Fig. 1(a). This suggests that the relative concentrations of As and P are similar in the solid and liquid phases at the growth temperature of  $600^\circ\text{C}$ . The crystals obtained in this way are much thinner than those obtained from the slow-cooling approach, and have a cracked-looking surface, but exploring the intrinsic magnetic trends is best done using these homogeneous crystals, and small  $\text{EuCuAs}_{1-x}\text{P}_x$  crystals are sufficient due to the large Eu moment.

X-ray diffraction data for select  $\text{EuCuAs}_{1-x}\text{P}_x$  samples are shown in Fig. 1(b). These results were obtained after grinding approximately 0.06 g of crystals, which contained a significant portion (10–15 mass percent) of Sn. The main phase is well fitted using a Rietveld refinement to the expected hexagonal structure. The peak positions evolve smoothly, as illustrated for the 202 Bragg reflection in the inset of Fig. 1(b). This trend demonstrates the evolution of the lattice parameters with composition, which is summarized in Table I. In Fig. 1(c), the refined lattice volumes are plotted versus the experimental  $x$  values and a linear relation is observed (Vegard's law appears to hold).

The lower panel of Fig. 1(c) plots the quantity  $c/a/2$ , which is equal to ratio of the Eu-Eu distance along  $c$  to that perpendicular to  $c$  (within the triangular array). This ratio is less than unity for all compositions, which shows that the Eu-Eu distance along the  $c$  axis is the shortest Eu-Eu distance. This ratio deviates from unity the most for EuCuAs and trends

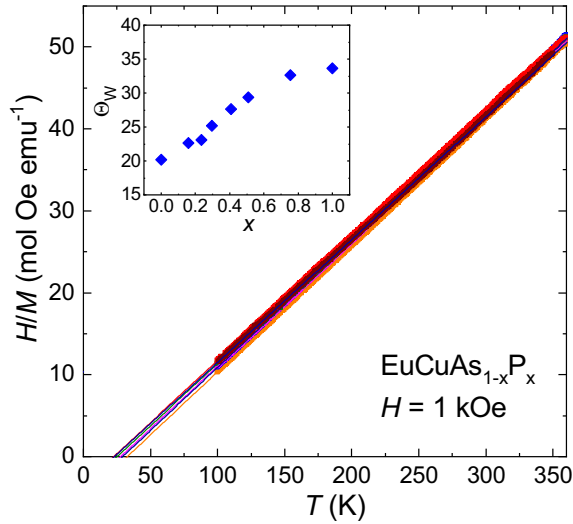


FIG. 2. (a) High-temperature magnetization data plotted as inverse susceptibility  $H/M$  with solid lines computed from a Curie-Weiss fit to  $\chi(T) = C/(T - \Theta_W)$  that produced the Curie-Weiss temperatures ( $\Theta_W$ ) in the inset;  $\Theta_W$  values for EuCuP and EuCuAs are also included.

toward unity upon increasing  $x$ . For comparison, in EuCuSb, the  $c$  axis is further expanded and the ratio is slightly less than 0.95 [55]. These materials thus have strong three-dimensional character with the relative separation between triangular Eu “planes” increasing upon increasing the mass of the pnictide.

### B. Magnetic properties of $\text{EuCuAs}_{1-x}\text{P}_x$ single crystals

We begin by providing a high-level summary of the magnetization ( $M$ ) data. At high temperatures, the samples behave as local moment paramagnets with dominant ferromagnetic correlations, as seen in Fig. 2(a). The magnetic transition temperatures are gradually enhanced as P is added to antiferromagnetic EuCuAs in the  $\text{EuCuAs}_{1-x}\text{P}_x$  crystals, as shown in the magnetization data of Figs. 3(a) and 3(b) and via specific heat ( $C_P$ ) data in Fig. 3(c). Compositions with  $x = 0.16$  and  $0.24$  likely have easy-plane antiferromagnetic ground states, similar to EuCuAs, while the phosphorous rich crystals ( $x \geq 0.41$ ) appear ferromagnetic like EuCuP. However, near  $\text{EuCuAs}_{0.75}\text{P}_{0.25}$  (consider the  $x = 0.24$  and  $0.30$  samples) the crystals display more complex magnetic behavior with multiple transitions as a function of temperature (Fig. 4), suggesting a competition between ground states. This more complex region is thus a clear feature of the phase diagram shown in Fig. 5. The isothermal magnetization data shown in Fig. 6 reveal a reduced magnetic anisotropy in the alloys, with compositions close to the  $x = 0, 1$  parent compounds maintaining the parent’s type of magnetic anisotropy.

Figure 2 presents the inverse susceptibility ( $1/\chi = H/M$ ) versus temperature for powder  $\text{EuCuAs}_{1-x}\text{P}_x$  samples. Included in the plot of  $1/\chi$  are lines from fitting  $\chi(T)$  to a Curie-Weiss law in the range 100–360 K; fitting that allowed a temperature-independent  $\chi_0$  term was also inspected and the results were qualitatively similar but the fit quality was not notably different. These data were collected on pulverized crystals and the diffraction data for these powders revealed

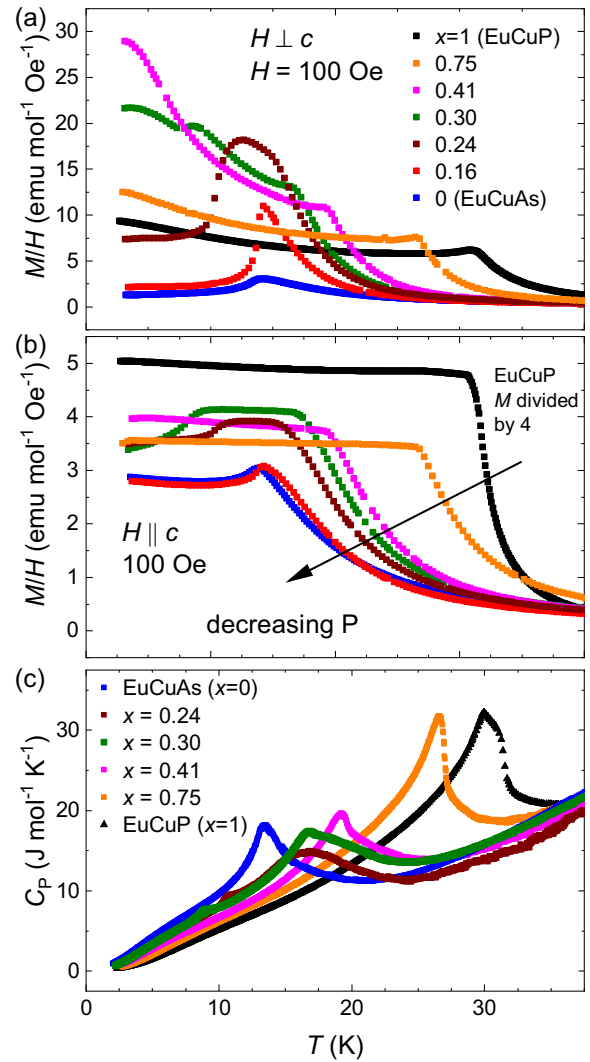


FIG. 3. Anisotropic magnetization data near the magnetic transitions of  $\text{EuCuAs}_{1-x}\text{P}_x$  crystals for (a)  $H \perp c$  and (b)  $H \parallel c$ . Note that the data for EuCuP in panel (b) are scaled to fit on the same  $y$  axis as the other compositions. (c) Specific heat capacity of select compositions in the region near the magnetic transitions for  $H = 0$ .

significant amounts of Sn, an issue which is exacerbated by the small crystal size and cracked surfaces. Such Sn contamination causes the mols of the magnetic component to be overestimated, and thus the magnetization (susceptibility) and effective moments obtained from the fitting are lower than expected for divalent Eu and are not provided. The Curie-Weiss temperatures, however, can be extracted with reasonable accuracy and they trend smoothly with  $x$ , as shown in the inset. The results are also tabulated in Table I. The results for EuCuP and EuCuAs were obtained using single crystals from Ref. [52]; the data were for  $H \parallel c$  and the data for EuCuAs were limited to 300 K.

The fitted Curie-Weiss temperatures are all positive, indicating dominant ferromagnetic correlations in the paramagnetic state. This is a common feature for many related materials containing triangular sublattices of Eu, including isostructural EuCuSb, EuAuSb, and EuAgSb [33]. With the

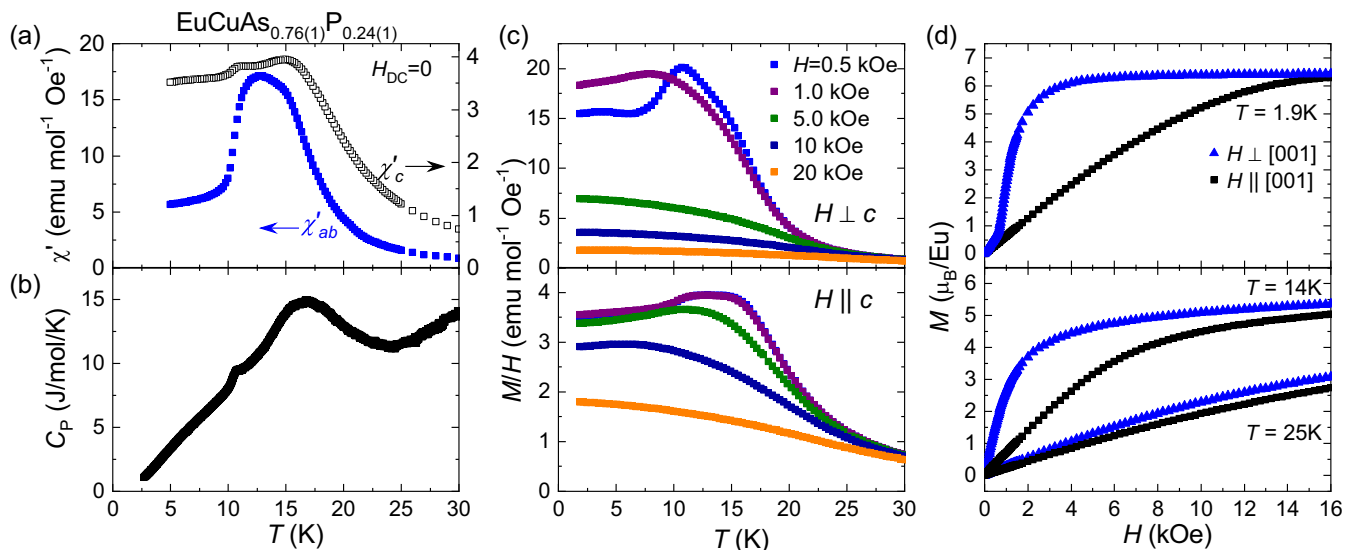


FIG. 4. Thermodynamic data for a crystal with  $x = 0.24$ . (a) In-phase ac susceptibility with the out-of-plane response on the right-side axis and the in-plane susceptibility on the left-side axis. (b) Specific heat capacity data in zero field. (c) DC magnetization versus temperature in different applied fields and (d) isothermal DC magnetization at select temperatures. The metamagnetic transition observed below 1 kOe for  $H \perp c$  in panel (d) evidences the easy-plane antiferromagnetic ground state for  $x = 0.2$ .

largest unit cell volume in this hexagonal family, EuCuBi is the only EuCuPn to possess a negative Curie-Weiss temperature [33,46]. In a simplistic view, the large ferromagnetic interactions seem to promote ferromagnetic coupling within the triangular array, and then the long-range magnetic order is determined by how these "layers" are coupled along the  $c$  axis, the direction along which the Eu-Eu distance is shortest.

Magnetization data near the magnetic transitions are shown in Figs. 3(a) and 3(b). A fairly smooth evolution of the transition temperatures and the qualitative shapes of the  $M(T)$  curves is observed for these samples, especially for large  $x$ . For instance, a cusp near  $T_C$  is observed in EuCuP for  $H \perp c$ , followed by a slight rise upon cooling. For  $H \parallel c$ , the low-field magnetic response is a sharp rise in the magnetization at  $T_C$  with essentially a plateau at lower temperatures; note the data for EuCuP in Fig. 3(b) are scaled. This behavior is retained upon decreasing phosphorus content to EuCuAs<sub>0.25</sub>P<sub>0.75</sub> ( $x = 0.75$ ), though the net magnetization for  $H \parallel c$  is greatly reduced in the EuCuAs<sub>1-x</sub>P<sub>x</sub> crystals. Low-field magnetization that is qualitatively similar to that in EuCuP is also observed for EuCuAs<sub>0.59</sub>P<sub>0.41</sub> ( $x = 0.41$ ), which is surprising given the large arsenic concentration in this sample. However, the rise in  $M$  upon cooling below the transition is substantial for  $x = 0.41$  when  $H \perp c$ . Additionally, this low-field  $M/H$  is larger than that in EuCuP, likely indicating reduced anisotropy.

Signatures of the competing antiferromagnetic order have emerged by EuCuAs<sub>0.70</sub>P<sub>0.30</sub> ( $x = 0.30$ ). For instance,  $M(T)$  decreases upon cooling below 8.6 K for  $H \parallel c$  in the  $x = 0.30$  sample. This indicates some compensation of the moments, perhaps with an easy-axis-like behavior, though signatures of a metamagnetic transition for  $H \parallel c$  were not observed in these samples. Similar behavior is observed in EuCuAs<sub>0.76</sub>P<sub>0.24</sub> ( $x = 0.24$ ) with a decreasing  $M(T)$  upon cooling below 10.6 K for both field orientations. As phosphorous content is reduced further, to EuCuAs<sub>0.84</sub>P<sub>0.16</sub> ( $x = 0.16$ ), a strong cusp

associated with antiferromagnetic order is observed when  $H \perp c$ . This is qualitatively similar to the behavior observed in EuCuAs. From these results, it appears that small additions of P into EuCuAs, or As into EuCuP, result in somewhat simple rescaling of the ordering temperatures and perhaps the magnetic anisotropy. However, a clear competition of different magnetic phases is observed for the intermediate compositions of  $x = 0.24$  and  $0.30$ . As such, the behavior for  $x = 0.24$  is examined in greater detail below (see Fig. 4).

Specific heat measurements were performed on select compositions to complement the magnetization measurements and

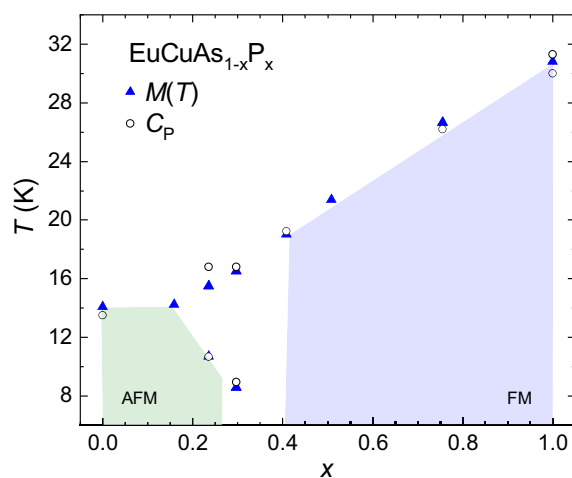


FIG. 5. Transition temperatures of EuCuAs<sub>1-x</sub>P<sub>x</sub> crystals estimated from magnetization data ( $H = 0.1$  kOe) and the specific heat capacity ( $H = 0$ ) plotted versus the experimental  $x$  values. The shaded regions indicate the speculated nature of the magnetic ground states (AFM, FM) based on magnetization measurements, while additional samples and measurements are needed to better refine the phases and boundaries in the unshaded central region.

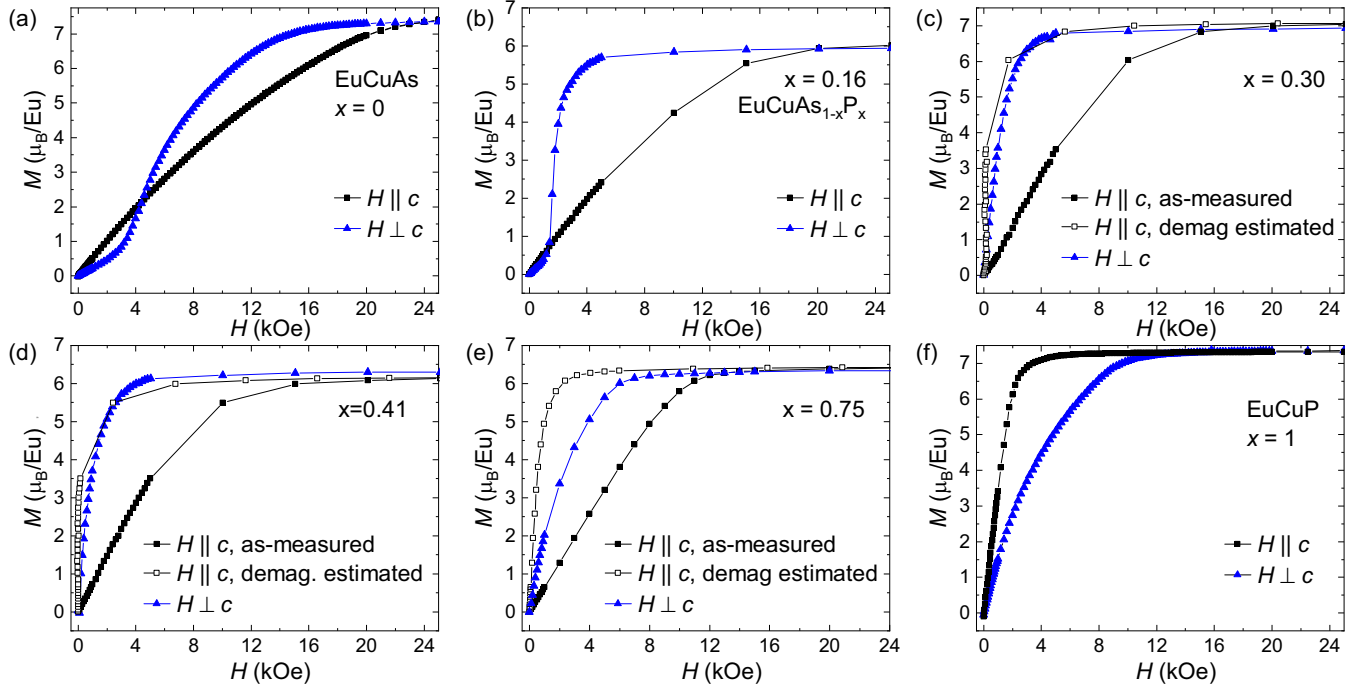


FIG. 6. Isothermal magnetization data at  $T = 2$  K for  $\text{EuCuAs}_{1-x}\text{P}_x$  crystals. The metamagnetic transitions when  $H \perp c$  for  $\text{EuCuAs}$  (a) and  $\text{EuCuAs}_{0.84}\text{P}_{0.16}$  (b) demonstrate easy-plane, antiferromagnetic ground states. The anisotropy in the other alloy crystals is not directly apparent and demagnetization effects are likely important. The open markers in (c) through (e) are shown after correcting for an estimate of the demagnetization field as discussed in the text. The data reveal that  $x = 0.75$  likely has easy-axis anisotropy and the remaining alloy compositions have very little anisotropy. In (f), the easy-axis anisotropy of  $\text{EuCuP}$  is directly evident because a thick crystal was mechanically shaped to eliminate the geometrical impact on the observed anisotropy [52].

the data are presented in Fig. 3(c). The characteristic temperatures observed in Fig. 3(c) are plotted along with those obtained from magnetization measurements to produce the phase diagram shown in Fig. 5.

Ferromagnetic  $\text{EuCuP}$  has two features in the anomaly near  $T_C = 31$  K, which were also observed in dilatometry experiments and confirmed on multiple samples [52]. In  $C_p$ , the higher temperature feature appears as a shoulder. For the alloy sample with  $x = 0.75$ , the peak is sharper without a clear shoulder, and as a result the jump in  $C_p$  at  $T_C$  is slightly larger (consider not the magnitude of  $C_p$  but the value relative to the expected background). As the phosphorous content is reduced, the specific heat anomaly broadens and the maximum is suppressed. This is the case for the  $x = 0.41$  sample, which has a peak shape like that of  $\text{EuCuAs}$  with perhaps a greater broadening on the high-temperature side. Significant broadening and suppression of the specific heat anomaly are observed for  $x = 0.24$  and  $x = 0.30$ ; the datasets for these samples also contain a small feature at lower temperature that is sharper than the dominant anomaly observed at higher temperatures. Given the relatively peculiar behavior observed near  $x = 0.25$ , we have provided a more detailed characterization of the  $x = 0.24$  sample in Fig. 4 and discuss those results next.

A detailed characterization of the magnetic properties of a crystal with composition  $\text{EuCuAs}_{0.76}\text{P}_{0.24}$  ( $x = 0.24$ ) was performed to assess the behavior in the arsenic-rich intermediate compositions. Figure 4 summarizes the properties for this crystal; dc magnetization data of a second crystal from

this same growth batch were found to be in agreement. Two transitions are observed in the ac susceptibility data shown in Fig. 4(a) and in the specific heat capacity data that are repeated from Fig. 3(c). Frequency dependence of the features in  $\chi'$  was not observed between 227 and 996 Hz for the ac measurements, suggesting a spin-glass state is not the ground state, though further measurements would be necessary to rule out any dynamic component.

As shown in Figs. 4(a) and 4(c), the anomaly in the susceptibility near 16 K is more prominent in the  $c$ -axis magnetization data, while that near 10.6 K impacts the in-plane susceptibility to a larger extent. The feature at higher temperature is not particularly sharp in any of these measurements. Based on the magnetization data, both anomalies are suppressed by applied field, consistent with antiferromagnet behavior. As shown in Fig. 4(d), a metamagnetic transition is observed for  $H \perp c$  at  $T = 1.9$  K but not at  $T = 14$  K (below the first anomaly). This may indicate a spin reorientation upon cooling and further evidences a clear difference between the ground state and the intermediate-temperature magnetic state. The question then becomes, "what is the nature of the transition near 17 K?". It is perhaps useful to consider related phases that display frustrated magnetism.  $\text{EuCuSb}$  also possesses two transitions as a function of temperature and the response in the magnetization data bears similarity in that the features at the critical temperatures are not sharp. Specific heat data were not reported for  $\text{EuCuSb}$  and a direct comparison is difficult to make. In  $\text{EuCuSb}$ , the transitions are from the paramagnetic state to a collinear spin structure with a propagation vector of

$(0, 0, \frac{1}{2})$  and then at lower temperature, an incommensurate  $c$ -axis helix competes with the collinear phase [51]. In addition, the collinear structure is reported to have easy-axis anisotropy while the helical structure has easy-plane anisotropy, and this may be a key aspect of the phase competition. A competition of the magnetic anisotropy is naturally present in these alloy samples due to the different anisotropy of EuCuAs and EuCuP. Given that an easy-plane  $c$ -axis helix is the ground state in EuCuAs, a similar ground state for the arsenic-rich alloys near  $x = 0.24$  would not be surprising, but the nature of these phases would need to be confirmed by neutron or resonant x-ray diffraction measurements.

The ordering temperatures are plotted versus composition in Fig. 5. The temperatures were selected from magnetization data using the cusp in  $M(T)$  for  $H \perp c$  observed in Fig. 3(a); for  $x = 0.24$  and  $0.30$ , which possess two features as a function of temperature, magnetization data for both orientations were inspected to best estimate the characteristic temperatures. The maxima in the specific heat data were also utilized, and for most compositions these temperatures coincide nicely. However, this is not the case for the  $x = 0.24$  sample where the broad peak in the specific heat is centered at  $T$  greater than the characteristic temperatures observed via magnetization. In addition, a small difference in these two methods is obtained for both parent compounds. Regardless of the quantitative details, the qualitative behavior is clear: transition temperatures trend nicely with  $x$  for most of the alloy series, but competing states exist near  $x = 0.25$  that result in a more complicated phase evolution. Further inspection of samples in this compositional space may reveal interesting magnetic states paired with complex transport properties. Care must be taken to ensure homogeneity when studying such samples.

We now consider the magnetic anisotropy in these materials, meaning the preferred orientation of the moments in the ground state  $H = 0$  spin structure. This aspect is considered via the isothermal  $M(H)$  data presented in Fig. 6. For these hexagonal systems, the simplest characterization is whether the crystals have easy-axis (moments along [001]) or easy-plane (moments perpendicular to [001]) anisotropy. For antiferromagnets like EuCuAs, the easy-plane anisotropy can be inferred from the existence of a metamagnetic transition occurring for  $H \perp c$ , as observed in Fig. 6(a). Therefore, the demagnetization effect does not need to be considered when attempting to determine the magnetic anisotropy. In such AFM cases, the anisotropy is also observed in the temperature-dependent magnetization data. As seen in Fig. 3, the magnetization decreases upon cooling below  $T_N$  when the field is applied within the basal plane whereas it is relatively independent of temperature when the field is applied along the  $c$  axis.

In EuCuAs, the metamagnetic transition is between a  $c$ -axis helix with in-plane moments for  $H = 0$  and a field-induced transverse conical spin structure that is noncoplanar and noncollinear [50]. This conical structure is characterized by an incommensurate  $(0,0,0.35)$  propagation vector, with the moment orientation rotating between parallel and perpendicular to [001]. Even for simpler metamagnetic transitions, such as a spin-flip (spin-flop) transition from a collinear magnetic structure to a canted (or polarized) one, the presence of the

metamagnetic transition generally indicates the existence of a preferred moment orientation.

When a metamagnetic transition is not observed, the anisotropy can be more difficult to determine, such as for ferromagnetic EuCuP. Indeed, even the type of magnetic order can become difficult to infer since the magnetocrystalline anisotropy and ordered moment possess different temperature dependence [56], which can lead to a peak in the susceptibility near a ferromagnetic transition (especially for the magnetically hard orientation). One complication in determining the anisotropy is the impact of demagnetization effects, which can be very important in large moment systems like these with  $S=7/2$  moments. This is especially true for  $H \parallel c$  in platelike crystals, such as those produced by the isothermal growth employed here. To keep the plots simple and to emphasize the qualitative behaviors that we are interested in, we elected to only show the estimated impact of demagnetization fields for samples where the anisotropy is unclear due to the absence of a metamagnetic transition combined with measurements on thin plates obtained from isothermal growths. For EuCuP, we previously reported data obtained using a blocky, three-dimensional crystal where the geometric demagnetization factor is similar for both orientations, and thus the sample geometry does not impact the determination of the easy-axis anisotropy when examining the isothermal magnetization data in Fig. 6(f). Precise determination of the demagnetization effect is challenging, especially for irregular crystals, thus we took the approach of illustrating the potential impact by using a geometry factor of  $N = 0.75$  and the crystallographic densities from Rietveld refinements at the experimental  $x$  values for the thin plate alloy crystals [57]. An illustration of the impact sample geometry can have on such large moment systems was provided for EuCuP in Ref. [52].

As shown in Fig. 6(b), the magnetic order and anisotropy of EuCuAs appears to be maintained for small  $x$  as in EuCuAs<sub>0.84</sub>P<sub>0.16</sub> ( $x = 0.16$ ). However, the critical field of the metamagnetic transition is reduced for  $x = 0.16$  compared to EuCuAs, suggesting a reduction in the magnetic anisotropy. The metamagnetic transition for  $x = 0.16$  looks sharper than in EuCuAs, though this may be the consequence of a different field-induced state since saturation seems to be rapidly approached for  $x = 0.16$ . As shown in Fig. 4, a metamagnetic transition was also observed for EuCuAs<sub>0.76</sub>P<sub>0.24</sub> ( $x = 0.24$ ) when  $H \perp c$  at  $T = 1.9$  K, evidencing an easy-plane anisotropy in the ground state up to at least  $x = 0.24$  in this solid solution.

For phosphorous content starting near  $x = 0.30$  (EuCuAs<sub>0.70</sub>P<sub>0.30</sub>), clear signatures of metamagnetic transitions are not present at 2 K and the anisotropy appears to be small and difficult to determine due to demagnetization effects. A further increase in phosphorous content to  $x = 0.41$  appears to produce a ferromagnetic or similar state with only one dominant transition temperature. For  $x = 0.41$  and  $0.75$ , the magnetic anisotropy is small and difficult to accurately determine due to demagnetization effects. However, it seems plausible that EuCuAs<sub>1-x</sub>P<sub>x</sub> samples near these phosphorous-rich compositions are easy-axis ferromagnets. Small anisotropy is anticipated in these alloys, in part because of the different anisotropy of the  $x = 0, 1$  parent compounds, and also because of the quenched orbital

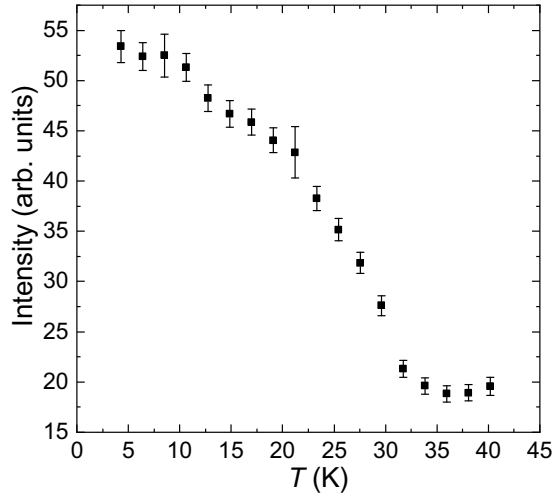


FIG. 7. Integrated intensity of the 010 Bragg reflection obtained by neutron diffraction on a single crystalline sample of EuCuP revealing an increasing magnetic scattering intensity on cooling below  $T_C \approx 31$  K; all observed diffraction intensity was consistent with ferromagnetic order.

moment ( $L = 0$ ) for divalent Eu in the free ion setting. The saturated moments are generally consistent with divalent Eu, though in some cases an artificially low saturation moment is obtained due to Sn contamination. Contamination by Sn was verified to be the source for this error through a separate etching test as well as by refinement of 1015 mass % of Sn in the powder x-ray diffraction.

### C. Neutron diffraction results on EuCuP

In this Section, we briefly report results from neutron single crystal diffraction data for EuCuP. The purpose of the measurement was to inspect for signatures of magnetic order beyond ferromagnetism, as motivated in part by the two features in the specific heat and dilatometry measurements near the Curie temperature. No evidence for such magnetic order was observed at  $T = 5$  K, where a full data set were collected and all the magnetic scattering was observed to be top of the crystallographic (nuclear) Bragg peaks. This indicates that the observed scattering is consistent with ferromagnetic order.

After collecting a full dataset at base temperature, the intensity of the 010 reflection was measured as a function of temperature. The integrated intensity is plotted versus temperature in Fig. 7. The data are consistent with the bulk Curie temperature near 31 K and a smooth evolution of the intensity with temperature is observed within the error bars. With the moments along [001], magnetic scattering intensity is observed in Bragg reflections containing a component perpendicular to [001], thus a strong magnetic intensity is observed at the 010 reflection. The data did not provide any evidence for a canting of the moment away from [001] at  $T = 5$  K.

The neutron diffraction data for EuCuP were collected on the TOPAZ single-crystal neutron time-of-flight Laue diffractometer [58] at the Spallation Neutron Source (SNS), Oak Ridge National Laboratory. A cube-shaped crystal of EuCuP measuring  $1.0 \text{ mm} \times 1.0 \text{ mm} \times 1.1 \text{ mm}$  was affixed to a custom-built aluminum pin with SuperGlue and mounted on

the TOPAZ goniometer. A custom-built cryogen-free TOPAZ Cryogoniometer with a Cryomech P415 pulse tube cryocooler was used for precise sample placement and temperature control. The EuCuP crystal is highly absorbing, with absorption coefficients  $\mu = 0.0342 + 7.544\lambda \text{ mm}^{-1}$ . CrystalPlan [59] was employed for peak placement on the detectors in reflection mode to minimize the effect from sample absorption in the variable temperature study, which was conducted with a heating rate of 0.5 K per minute from  $\approx 5$  K to 40 K. Data reduction and normalization followed established procedures [60,61].

## IV. SUMMARY

Materials with the hexagonal ZrBeSi structure type, and related systems with slight distortions, display interesting magnetic and electronic properties. This manuscript focused on alloys between helimagnetic EuCuAs and ferromagnetic EuCuP. A key feature in this alloy system is the changing anisotropy, with easy-axis anisotropy in EuCuP and easy-plane moments in EuCuAs. Both systems share positive Curie-Weiss temperatures, as do the EuCuAs $_{1-x}$ P $_x$  samples where the Curie-Weiss temperatures evolve rather smoothly with composition (lattice volume). In the EuCuAs $_{1-x}$ P $_x$  samples with large phosphorous contents ( $x \geq 0.41$ ), behavior similar to the ferromagnetism in EuCuP is observed, albeit with what appears to be a reduced anisotropy. For phosphorous content such as EuCuAs $_{0.84}$ P $_{0.16}$  ( $x = 0.16$ ), behavior qualitatively similar to that of EuCuAs is observed, indicating easy-plane antiferromagnetic ground states. In these alloy crystals, the anisotropy is reduced and this might have consequences for the formation of the field-induced conical spin structure observed in EuCuAs. More complex behavior is observed in the samples with arsenic content near  $x = 0.25$ . Specifically, for EuCuAs $_{0.76}$ P $_{0.24}$  and EuCuAs $_{0.70}$ P $_{0.30}$  there are two magnetic transitions as a function of temperature, indicating a competition of the magnetic ground states. This behavior may originate from a competition of the magnetic anisotropy (a spin reorientation upon cooling), which appears to be a component of the frustration that leads to two transitions in the isostructural material EuCuSb. An interesting coupling of the magnetism and the transport properties is expected in the region near  $x = 0.25$ , though great care must be taken to obtain chemically homogeneous crystals if further investigations are pursued. In this work, an isothermal flux growth was utilized to avoid the inhomogeneity that was found in crystals grown using a slow-cooling flux method. Isothermal growths may prove useful for many alloy systems, though the crystal size and morphology is likely to be negatively impacted and optimization of an isothermal growth may be more challenging.

## ACKNOWLEDGMENTS

This work was supported by the U. S. Department of Energy, Office of Science, Basic Energy Sciences, Materials Sciences and Engineering Division. A portion of this research used resources at the Spallation Neutron Source, a DOE Office of Science User Facility operated by the Oak Ridge National Laboratory. We thank J. Yan and M. McGuire for useful discussions.



- [1] B. A. Bernevig, C. Felser, and H. Beidenkopf, Progress and prospects in magnetic topological materials, *Nature (London)* **603**, 41 (2022).
- [2] Y. Tokura and N. Kanazawa, Magnetic skyrmion materials, *Chem. Rev.* **121**, 2857 (2021).
- [3] X. Zhang, Y. Zhou, K. M. Song, T.-E. Park, J. Xia, M. Ezawa, X. Liu, W. Zhao, G. Zhao, and S. Woo, Skyrmion-electronics: Writing, deleting, reading and processing magnetic skyrmions toward spintronic applications, *J. Phys.: Condens. Matter* **32**, 143001 (2020).
- [4] C. H. Marrows and K. Zeissler, Perspective on skyrmion spintronics, *Appl. Phys. Lett.* **119**, 250502 (2021).
- [5] H. Zhang, Y. Zhang, Z. Hou, M. Qin, X. Gao, and J. Liu, Magnetic skyrmions: Materials, manipulation, detection, and applications in spintronic devices, *Mater. Futures* **2**, 032201 (2023).
- [6] L. Jiao, Q. Xu, Y. Cheon, Y. Sun, C. Felser, E. Liu, and S. Wirth, Signatures for half-metallicity and nontrivial surface states in the kagome lattice Weyl semimetal  $\text{Co}_3\text{Sn}_2\text{S}_2$ , *Phys. Rev. B* **99**, 245158 (2019).
- [7] N. Morali, R. Batabyal, P. K. Nag, E. Liu, Q. Xu, Y. Sun, B. Yan, C. Felser, N. Avraham, and H. Beidenkopf, Fermi-arc diversity on surface terminations of the magnetic Weyl semimetal  $\text{Co}_3\text{Sn}_2\text{S}_2$ , *Science* **365**, 1286 (2019).
- [8] D. Liu, A. Liang, E. Liu, Q. Xu, Y. Li, C. Chen, D. Pei, W. Shi, S. Mo, and P. Dudin, Magnetic Weyl semimetal phase in a kagomé crystal, *Science* **365**, 1282 (2019).
- [9] A. Rossi, V. Ivanov, S. Sreedhar, A. L. Gross, Z. Shen, E. Rotenberg, A. Bostwick, C. Jozwiak, V. Taufour, S. Y. Savrasov, and I. M. Vishik, Electronic structure and topology across  $T_c$  in the magnetic Weyl semimetal  $\text{Co}_3\text{Sn}_2\text{S}_2$ , *Phys. Rev. B* **104**, 155115 (2021).
- [10] J.-Q. Yan, Q. Zhang, T. Heitmann, Z. Huang, K. Y. Chen, J.-G. Cheng, W. Wu, D. Vaknin, B. C. Sales, and R. J. McQueeney, Crystal growth and magnetic structure of  $\text{MnBi}_2\text{Te}_4$ , *Phys. Rev. Mater.* **3**, 064202 (2019).
- [11] S. H. Lee, Y. Zhu, Y. Wang, L. Miao, T. Pillsbury, H. Yi, S. Kempinger, J. Hu, C. A. Heikes, and P. Quarterman, Spin scattering and noncollinear spin structure-induced intrinsic anomalous Hall effect in antiferromagnetic topological insulator  $\text{MnBi}_2\text{Te}_4$ , *Phys. Rev. Res.* **1**, 012011 (2019).
- [12] D. Zhang, M. Shi, T. Zhu, D. Xing, H. Zhang, and J. Wang, Topological axion states in the magnetic insulator  $\text{MnBi}_2\text{Te}_4$  with the quantized magnetoelectric effect, *Phys. Rev. Lett.* **122**, 206401 (2019).
- [13] M. M. Otrokov, I. P. Rusinov, M. Blanco-Rey, M. Hoffmann, A. Y. Vyazovskaya, S. V. Ereemeev, A. Ernst, P. M. Echenique, A. Arnau, and E. V. Chulkov, Unique thickness-dependent properties of the van der Waals interlayer antiferromagnet  $\text{MnBi}_2\text{Te}_4$  films, *Phys. Rev. Lett.* **122**, 107202 (2019).
- [14] J. Li, Y. Li, S. Du, Z. Wang, B.-L. Gu, S.-C. Zhang, K. He, W. Duan, and Y. Xu, Intrinsic magnetic topological insulators in van der Waals layered  $\text{MnBi}_2\text{Te}_4$ -family materials, *Sci. Adv.* **5**, eaaw5685 (2019).
- [15] K. He,  $\text{MnBi}_2\text{Te}_4$ -family intrinsic magnetic topological materials, *npj Quantum Mater.* **5**, 90 (2020).
- [16] M. M. Otrokov, I. I. Klimovskikh, H. Bentmann, D. Estyunin, A. Zeugner, Z. S. Aliev, S. Gaß, A. Wolter, A. Koroleva, and A. M. Shikin, Prediction and observation of an antiferromagnetic topological insulator, *Nature (London)* **576**, 416 (2019).
- [17] A. M. Goforth, P. Klavins, J. C. Fettinger, and S. M. Kauzlarich, Magnetic properties and negative colossal magnetoresistance of the rare earth zintl phase  $\text{EuIn}_2\text{As}_2$ , *Inorg. Chem.* **47**, 11048 (2008).
- [18] Y. Xu, Z. Song, Z. Wang, H. Weng, and X. Dai, Higher-order topology of the axion insulator  $\text{EuIn}_2\text{As}_2$ , *Phys. Rev. Lett.* **122**, 256402 (2019).
- [19] Y. Zhang, K. Deng, X. Zhang, M. Wang, Y. Wang, C. Liu, J.-W. Mei, S. Kumar, E. F. Schwier, K. Shimada, C. Chen, and B. Shen, In-plane antiferromagnetic moments and magnetic polaron in the axion topological insulator candidate  $\text{EuIn}_2\text{As}_2$ , *Phys. Rev. B* **101**, 205126 (2020).
- [20] S. X. Riberolles, T. V. Trevisan, B. Kuthanazhi, T. Heitmann, F. Ye, D. Johnston, S. Bud'ko, D. Ryan, P. Canfield, and A. Kreyssig, Magnetic crystalline-symmetry-protected axion electrodynamics and field-tunable unpinned Dirac cones in  $\text{EuIn}_2\text{As}_2$ , *Nat. Commun.* **12**, 999 (2021).
- [21] J. Yan, Z. Z. Jiang, R. C. Xiao, W. J. Lu, W. H. Song, X. B. Zhu, X. Luo, Y. P. Sun, and M. Yamashita, Field-induced topological Hall effect in antiferromagnetic axion insulator candidate  $\text{EuIn}_2\text{As}_2$ , *Phys. Rev. Res.* **4**, 013163 (2022).
- [22] M. Gong, D. Sar, J. Friedman, D. Kaczorowski, S. Abdel Razek, W.-C. Lee, and P. Aynajian, Surface state evolution induced by magnetic order in axion insulator candidate  $\text{EuIn}_2\text{As}_2$ , *Phys. Rev. B* **106**, 125156 (2022).
- [23] J.-R. Soh, F. de Juan, M. G. Vergniory, N. B. M. Schröter, M. C. Rahn, D. Y. Yan, J. Jiang, M. Bristow, P. Reiss, J. N. Blandy, Y. F. Guo, Y. G. Shi, T. K. Kim, A. McCollam, S. H. Simon, Y. Chen, A. I. Coldea, and A. T. Boothroyd, Ideal Weyl semimetal induced by magnetic exchange, *Phys. Rev. B* **100**, 201102 (2019).
- [24] L.-L. Wang, N. H. Jo, B. Kuthanazhi, Y. Wu, R. J. McQueeney, A. Kaminski, and P. C. Canfield, Single pair of Weyl fermions in the half-metallic semimetal  $\text{EuCd}_2\text{As}_2$ , *Phys. Rev. B* **99**, 245147 (2019).
- [25] N. H. Jo, B. Kuthanazhi, Y. Wu, E. Timmons, T.-H. Kim, L. Zhou, L.-L. Wang, B. G. Ueland, A. Palasyuk, D. H. Ryan, R. J. McQueeney, K. Lee, B. Schruck, A. A. Burkov, R. Prozorov, S. L. Bud'ko, A. Kaminski, and P. C. Canfield, Manipulating magnetism in the topological semimetal  $\text{EuCd}_2\text{As}_2$ , *Phys. Rev. B* **101**, 140402 (2020).
- [26] S. Roychowdhury, M. Yao, K. Samanta, S. Bae, D. Chen, S. Ju, A. Raghavan, N. Kumar, P. Constantinou, and S. N. Guin, Anomalous Hall conductivity and nernst effect of the ideal Weyl semimetallic ferromagnet  $\text{EuCd}_2\text{As}_2$ , *Adv. Sci.* **10**, 2207121 (2023).
- [27] A. F. May, M. A. McGuire, and B. C. Sales, Effect of Eu magnetism on the electronic properties of the candidate Dirac material  $\text{EuMnBi}_2$ , *Phys. Rev. B* **90**, 075109 (2014).
- [28] H. Masuda, H. Sakai, M. Tokunaga, Y. Yamasaki, A. Miyake, J. Shiogai, S. Nakamura, S. Awaji, A. Tsukazaki, and H. Nakao, Quantum Hall effect in a bulk antiferromagnet  $\text{EuMnBi}_2$  with magnetically confined two-dimensional Dirac fermions, *Sci. Adv.* **2**, e1501117 (2016).
- [29] R. A. Susilo, W. Deng, J. Feng, A. Wang, N. Kawamura, N. Ishimatsu, S. Kawaguchi, M. Yuan, H. Li, W. Ren, T. Nakagawa, C. Petrovic, and B. Chen, Impacts of pressure

- to the structural, electronic and magnetic properties of Dirac semimetal EuMnBi<sub>2</sub>, *Phys. Rev. Res.* **3**, 043028 (2021).
- [30] H. Nishiyama, H. Sakai, K. Nakagawa, N. Hanasaki, S. Ishiwata, H. Masuda, M. Ochi, K. Kuroki, S. Iguchi, T. Sasaki, Y. Ikemoto, T. Moriwaki, K. Ueda, Y. Tokura, and J. Fujioka, Variation of charge dynamics upon antiferromagnetic transitions in the Dirac semimetal EuMnBi<sub>2</sub>, *Phys. Rev. B* **104**, 115111 (2021).
- [31] X. Gui, I. Pletikoscic, H. Cao, H.-J. Tien, X. Xu, R. Zhong, G. Wang, T.-R. Chang, S. Jia, and T. Valla, A new magnetic topological quantum material candidate by design, *ACS Central Sci.* **5**, 900 (2019).
- [32] G. M. Pierantozzi, A. De Vita, C. Bigi, X. Gui, H.-J. Tien, D. Mondal, F. Mazzola, J. Fujii, I. Vobornik, and G. Vinai, Evidence of magnetism-induced topological protection in the axion insulator candidate EuSn<sub>2</sub>P<sub>2</sub>, *Proc. Natl. Acad. Sci.* **119**, e2116575119 (2022).
- [33] C. Tomuschat and H.-U. Schuster, Magnetische eigenschaften der verbindungsreihe EuBX mit B= element der ersten neben- und X= element der fünften hauptgruppe, *Z. Anorg. Allg. Chem.* **518**, 161 (1984).
- [34] R. Pöttgen and D. Johrendt, Equiatomic intermetallic europium compounds: Syntheses, crystal chemistry, chemical bonding, and physical properties, *Chem. Mater.* **12**, 875 (2000).
- [35] G. Michels, S. Junk, W. Schlabit, E. Holland-Moritz, M. Abd-Elmeguid, J. Dunner, and A. Mewis, Final-state effects in divalent Eu pnictides, *J. Phys.: Condens. Matter* **6**, 1769 (1994).
- [36] H.-J. Zhang, S. Chadov, L. Müchler, B. Yan, X.-L. Qi, J. Kübler, S.-C. Zhang, and C. Felser, Topological insulators in ternary compounds with a honeycomb lattice, *Phys. Rev. Lett.* **106**, 156402 (2011).
- [37] Y. Du, B. Wan, D. Wang, L. Sheng, C.-G. Duan, and X. Wan, Dirac and Weyl semimetal in XYBi (X= Ba, Eu; Y = Cu, Ag and Au), *Sci. Rep.* **5**, 14423 (2015).
- [38] C. K. Barman, C. Mondal, B. Pathak, and A. Alam, Symmetry-driven topological phases in XAgBi (X = Ba, Sr): An ab initio hybrid functional calculation, *Phys. Rev. Mater.* **4**, 084201 (2020).
- [39] Q. D. Gibson, L. M. Schoop, L. Muechler, L. S. Xie, M. Hirschberger, N. P. Ong, R. Car, and R. J. Cava, Three-dimensional Dirac semimetals: Design principles and predictions of new materials, *Phys. Rev. B* **91**, 205128 (2015).
- [40] B. Singh, S. Mardanya, C. Su, H. Lin, A. Agarwal, and A. Bansil, Spin-orbit coupling driven crossover from a starfruitlike nodal semimetal to Dirac and Weyl semimetal state in CaAuAs, *Phys. Rev. B* **98**, 085122 (2018).
- [41] S. Mardanya, B. Singh, S.-M. Huang, T.-R. Chang, C. Su, H. Lin, A. Agarwal, and A. Bansil, Prediction of threefold fermions in a nearly ideal Dirac semimetal BaAgAs, *Phys. Rev. Mater.* **3**, 071201 (2019).
- [42] H. Gao, J. W. Venderbos, Y. Kim, and A. M. Rappe, Topological semimetals from first principles, *Annu. Rev. Mater. Res.* **49**, 153 (2019).
- [43] K. Nakayama, Z. Wang, D. Takane, S. Souma, Y. Kubota, Y. Nakata, C. Cacho, T. Kim, S. A. Ekahana, M. Shi, M. Kitamura, K. Horiba, H. Kumigashira, T. Takahashi, Y. Ando, and T. Sato, Observation of inverted band structure in the topological Dirac semimetal candidate CaAuAs, *Phys. Rev. B* **102**, 041104 (2020).
- [44] Z. Hu, J. Koo, Y. Hu, Q. Wang, M. Abeykoon, D. Graf, Y. Liu, H. Lei, J. Ma, M. Shi, B. Yan, and C. Petrovic, Topological Dirac semimetal BaAuSb, *Phys. Rev. Res.* **5**, 013079 (2023).
- [45] Y. Jin, X.-T. Zeng, X. Feng, X. Du, W. Wu, X.-L. Sheng, Z.-M. Yu, Z. Zhu, and S. A. Yang, Multiple magnetism-controlled topological states in EuAgAs, *Phys. Rev. B* **104**, 165424 (2021).
- [46] X. Wang, B. Li, L. Zhou, L. Chen, Y. Wang, Y. Yang, Y. Zhou, K. Liao, H. Weng, and G. Wang, Structure, physical properties, and magnetically tunable topological phases in the topological semimetal EuCuBi, *Phys. Rev. B* **108**, 115126 (2023).
- [47] W. Iha, M. Kakihana, S. Matsuda, F. Honda, Y. Haga, T. Takeuchi, M. Nakashima, Y. Amako, J. Gouchi, and Y. Uwatoko, Anomalous ferromagnetic ordering in EuCuP, *J. Alloys Compd.* **788**, 361 (2019).
- [48] J. Wang, J. Shen, Y. Wang, T. Liang, X. Wang, R. Zu, S. Zhang, Q. Zeng, E. Liu, and X. Xu, Anisotropic magneto-transport behavior in a hexagonal ferromagnetic EuCuP single crystal, *J. Alloys Compd.* **947**, 169620 (2023).
- [49] J. Tong, J. Parry, Q. Tao, G.-H. Cao, Z.-A. Xu, and H. Zeng, Magnetic properties of EuCuAs single crystal, *J. Alloys Compd.* **602**, 26 (2014).
- [50] S. Roychowdhury, K. Samanta, P. Yanda, B. Malaman, M. Yao, W. Schnelle, E. Guilmeau, P. Constantinou, S. Chandra, and H. Borrmann, Interplay between magnetism and topology: Large topological Hall effect in an antiferromagnetic topological insulator, EuCuAs, *J. Am. Chem. Soc.* **145**, 12920 (2023).
- [51] H. Takahashi, K. Aono, Y. Nambu, R. Kiyonagi, T. Nomoto, M. Sakano, K. Ishizaka, R. Arita, and S. Ishiwata, Competing spin modulations in the magnetically frustrated semimetal EuCuSb, *Phys. Rev. B* **102**, 174425 (2020).
- [52] A. F. May, E. M. Clements, H. Zhang, R. P. Hermann, J. Yan, and M. A. McGuire, Coupling of magnetism, crystal lattice, and transport in EuCuP and EuCuAs, *Phys. Rev. Mater.* **7**, 064406 (2023).
- [53] P. C. Canfield, T. Kong, U. S. Kaluarachchi, and N. H. Jo, Use of frit-disc crucibles for routine and exploratory solution growth of single crystalline samples, *Philos. Mag.* **96**, 84 (2016).
- [54] J. Rodríguez-Carvajal, Recent advances in magnetic structure determination by neutron powder diffraction, *Phys. B: Condens. Matter* **192**, 55 (1993).
- [55] T. Mishra, I. Schellenberg, M. Eul, and R. Pöttgen, Structure and properties of EuTsb (T = Cu, Pd, Ag, Pt, Au) and YbIrSb, *Z. Kristallogr.* **226**, 590 (2011).
- [56] S. Nikolov, P. Nieves, A. P. Thompson, M. A. Wood, and J. Tranchida, Temperature dependence of magnetic anisotropy and magnetoelasticity from classical spin-lattice calculations, *Phys. Rev. B* **107**, 094426 (2023).
- [57] D.-X. Chen, E. Pardo, and A. Sanchez, Demagnetizing factors of rectangular prisms and ellipsoids, *IEEE Trans. Magn.* **38**, 1742 (2002).
- [58] L. Coates, H. Cao, B. C. Chakoumakos, M. D. Frontzek, C. Hoffmann, A. Y. Kovalevsky, Y. Liu, F. Meilleur, A. M. dos Santos, and D. A. Myles, A suite-level review of the neutron single-crystal diffraction instruments at oak ridge national laboratory, *Rev. Sci. Instrum.* **89**, 092802 (2018).
- [59] J. Zikovsky, P. F. Peterson, X. P. Wang, M. Frost, and C. Hoffmann, Crystalplan: An experiment-planning tool for crystallography, *J. Appl. Cryst.* **44**, 418 (2011).

- [60] T. M. Michels-Clark, A. T. Savici, V. E. Lynch, X. Wang, and C. M. Hoffmann, Expanding lorentz and spectrum corrections to large volumes of reciprocal space for single-crystal time-of-flight neutron diffraction, *J. Appl. Cryst.* **49**, 497 (2016).
- [61] A. T. Savici, M. A. Gigg, O. Arnold, R. Tolchenov, R. E. Whitfield, S. E. Hahn, W. Zhou, and I. A. Zaliznyak, Efficient data reduction for time-of-flight neutron scattering experiments on single crystals, *J. Appl. Cryst.* **55**, 1514 (2022).